Rezumat

Codul numeric T3ST este instrumentul nostru preferat pentru studierea transportului turbulent în tokamakuri. În această fază a proiectului, codul a suferit corecții și îmbunătățiri minore, împreună cu adăugarea de noi rutine pentru a reprezenta cu exactitate echilibrele magnetice și coliziunile. O serie de teste analitice, numerice și statistice au fost efectuate pentru a-i asigura acuratețea. Folosind acest cod, am generat o bază de date de simulări numerice prin variarea a 22 de parametri individual în jurul unui scenariu de referință.
Analiza complexă a aspectelor coerente din turbulență (Obiectivul A1) a relevat în statistica traiectoriilor ionilor în plasma turbulentă existența unor mișcări coerente ascunse. Acestea au un rol esențial în transport. O variație temporală slabă a potențialului generează în mod surprinzător timp lung de viață pentru mișcarea coerentă. Am arătat, folosind metoda modurilor test, că turbulența de drift este influențată de coerența traiectoriilor ionilor. În această etapă, am dezvoltat un cod care combină calcule de particule test și de moduri test într-o metodă iterată. Acesta este o unealtă utilă pentru înțelegerea efectelor complexe ale coerenței traiectoriilor asupra evoluției turbulenței.

Summary

The T3ST numerical code is our preferred tool for studying turbulent transport in tokamaks. In this phase of the project, the code underwent minor corrections and improvements, along with the addition of new routines for accurately representing magnetic equilibria and collisions. A series of analytical, numerical, and statistical tests have been conducted to ensure its accuracy. Using this code, we generated a database of numerical simulations by varying 22 parameters individually around a baseline scenario. The deep analysis of the coherent aspects in turbulence (Objective A1) has revealed hidden coherent motion in the statistics of ion trajectories in turbulent plasmas, which has an essential role in the transport. Unexpectedly, a slow time variation of the potential generates long lifetime of the coherent motion. We have also shown, using test mode approach, that ion trajectory coherence influences the drift turbulence. In the present stage, a code that combines test particle and test mode calculations in an iterated approach was developed. It is a very useful tool for understanding the complex effects of trajectory coherence on turbulence evolution.

Self-consistent code for turbulence evolution. Database of simulations for the analysis of the experimental results on fluctuations and turbulent transport.

A. Self-consistent code for turbulence evolution

One of the aims included in this topic is of fundamental nature and consists of a deep analysis of one of the main aspects of strong turbulence: the high degree of coherence. More precisely, this project focuses on the validation and development of predictions obtained in previous work on the existence of hidden coherent drifts (HDs) in the statistics of ion motion in turbulent states [1], and on their effects on transport [2,3]. They are based on the decorrelation trajectory method [4,5], an approximate semi-analytical approach. Significant contributions to the understanding of ion trajectory coherence and of the effects on transport and turbulence evolution were obtained during the first two years of the project.

The first stage (Deliverable A1) was dedicated to the identification of the hidden coherent components of the turbulent motion. The analysis was based on the numerical simulations of ion trajectories in a stochastic potentials, which were performed with the codes developed in our group [6-13]. It consists of deep statistical studies that determine the properties of classes of trajectories defined by the value of the initial potential φ^0 and by their topology (free and trapped). We have shown that an average velocity $\mathbf{V}_d$ superposed on the ExB drift determines important coherent effects, beside the HDs (a pair of average velocities perpendicular to $\mathbf{V}_d$ that compensate each other). Most of them are hidden in the sense that they do not determine average displacements or velocities, because their average over φ^0 is zero. However, the dispersion of the trajectories and the transport are essentially determined by the coherent displacements of the free trajectories. We have also shown that a slow time variation of the potential has not the expected effect of attenuation of the coherent component of the motion. A surprising effect of enhanced coherence appears, associated to long-time memory of the potential and of the stochastic vorticity.

The second stage (Deliverable A2) consists of a theoretical study of the test modes on turbulent plasmas in the case of drift type turbulence. The growth rates and the frequencies of the modes were determined as functions of the characteristics of the background turbulence. The main ingredient is the calculation of the propagator that is defined as an average on the stochastic ion trajectories. The original aspect is the use of the conditional Lagrangian statistics developed for the trajectories. It reveals the effects of the coherent components of the ion trajectories. The dispersion relation for the test modes is determined. It is much more complicated since it includes several statistical quantities that are taken into account for the first time. The long memory found in the statistics of trajectories (with characteristic time τ_m that is much larger than the correlation time of the Eulerian potential) determines growth rates and the frequencies of the modes that are intrinsically time-dependent. This causes an oscillating evolution of the turbulence with small frequencies of the order $1/\tau_m$. A second source of instability, which develops as the amplitude of the turbulence increases, was also found. It is determined by the HDs and other elements of the coherent motion.

The present stage (Deliverable A3) consists of developing of a numerical code based on the iterated self-consistent (ISC) approach for the study of the evolution of drift turbulence. A short description of the ISC approach and of the new elements introduced here is first presented. It is essentially a

sequence of repeated calculations of the test modes characteristics and of the test particle statistical quantities. Then details on these two main sections are discussed together with the development and improvements of the theoretical aspects.

The iterated self-consistent (ISC) approach

Test particle and test mode studies of turbulence start from the given statistical description of turbulence. They evaluate the growth rates of the modes, the diffusion coefficients and the characteristics of the transport as functions of the parameters of the background turbulence. They provide scaling and dependences of these quantities on the parameters of the turbulence models. Thus, the output of the test mode studies is completely different from that of the self-consistent studies, which determine the characteristics of the turbulence and of the transport, generated in given macroscopic conditions. However, we have shown [NJP] that a self-consistent evaluation of turbulence evolution can be constructed based on couplet studies of test particle and test modes. It is essentally enabled by the different characteristic times of the transport and of the evolution of the turbulence. The first is the decorrelation time of the stochastic potential that is produced by the drift with the diamagnetic velocity $\tau_* \cong 1/(k_2 V_{*e}) \cong 1/\omega$, while the second is of the order $\tau_c \cong 1/\gamma$. As $\gamma \ll \omega$, $\tau_c \gg \tau_*$.

The iterated self-consistent (ISC) approach was developed for the study of the drift turbulence in a model similar with the present one [NJP]. A simplified description permitted to derive analytical expressions for the test mode growth rates and frequencies. The coherence induced by the drift of the background potential was not known at that time. Also, the evaluation of the statistics of the test particles was performed with an approximate semi-analytical approach, the DTM. This study has shown that the ISC can obtain results qualitatively in agreement with those of the self-consistent simulations, and, most importantly, contributed to the understanding of some nonlinear processes in drift turbulence.

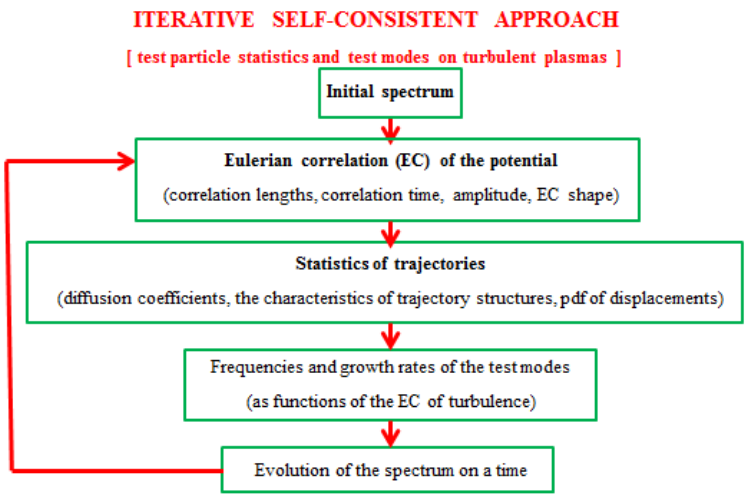

Figure 1 General schema of the ISC approach and code

The methodology of the ISC approach (Fig. 1) consists of repeated steps (after the initialisation of the background potential at a very small level with a large spectrum), which contain the following calculations.

- The evaluation of the characteristics of the turbulence from the spectrum (correlation lengths and time, amplitude, Eulerian correlation, characteristic times, transport regime)

- The calculation of the statistical characteristics of the trajectories that appear in the dispersion relation of the test modes (diffusion coefficients, probability of displacements, characteristics of the quasi-coherent structures) as functions of the turbulence spectrum – Test particle module

- The calculation of the renormalized propagator (conditional averaged over trajectories) and evaluation of the frequencies and the growth rates of the test modes – Test mode module

- The evolution of the spectrum on a small time interval is obtained using the growth rates of all modes. It is the starting point of a new step in this iterated method.

The main goal in the present study is to develop a code that is able to determine the effects of the coherence introduced by the average velocity (drift of the potential with the diamagnetic velocity) on the evolution of drift turbulence and the associated transport.

Significant improvements are introduced here. Most importantly, the test particle module is based on numerical simulation of the statistical ensemble of trajectories, such that the approximations of the DTM are eliminated. The deeper statistical analyses for both test particles and test modes yield much longer calculation and complex equation that have to be embedded in the code. Also, the number of statistical quantities that are necessary for the description of trajectory coherence is rather large. More details are presented below for the main modules of the code.

Test mode module

A significant simplification of the ion response function was introduced, which leads to a smaller number of statistical quantities in the dispersion relation.

The propagators in the ion response to test modes on turbulent plasmas

$$\bar{\Pi}_1^i = i\int_{-\infty}^{t} d\tau \langle M(\tau,t)\rangle \exp\left[-i\omega(\tau-t)\right] \tag{1}$$

$$\bar{\Pi}_2^i = i\int_{-\infty}^{t} d\tau \left\langle \left(k_i v_{ib}(\mathbf{x}(\tau)-\mathbf{V}_{*e}\tau)\right) M(\tau,t)\right\rangle \exp\left[-i\omega(\tau-t)\right] \tag{2}$$

depend on trajectories through the function $M(\tau)$

$$M(\tau,t) \equiv \exp\left[\frac{e\phi_b(\mathbf{x}-\mathbf{V}_{*e}t)}{T_e} + i\mathbf{k}\cdot(\mathbf{x}(\tau)-\mathbf{x}) - \int_\tau^t d\tau' \nabla\cdot\mathbf{u}_p\left(\mathbf{x}(\tau')\right)\right] \tag{3}$$

The compressibility term depends on the vorticity of the backward turbulence $\zeta(\mathbf{x},t) = \Delta\phi_b(\mathbf{x},t)$

$$\int_\tau^t d\tau' \nabla\cdot\mathbf{u}_p\left(\mathbf{x}(\tau')\right) = -\frac{m_i}{eB^2}\int_\tau^t d\tau'\, \partial_{\tau'}\zeta(\tau'). \tag{4}$$

Since the Lagrangian potential and vorticity have similar statistical properties, we introduce the combined stochastic function, which represents the gain of potential vorticity

$$\vartheta(\tau) = \varphi(\tau) - \varphi(0) - (\zeta(\tau) - \zeta(0)) \tag{5}$$

In terms of dimensionless quantities, Eq. (3) is

$$M(\tau,t) \equiv \exp\left[\frac{e\Phi}{T_e}\vartheta(\tau) + i\mathbf{k}\cdot(\mathbf{x}(\tau)-\mathbf{x})\right]. \quad (6)$$

The average of this stochastic function contains 8 statistical quantities (with 11 in the previous version).

The potential vorticity has a coherent component with long time memory. It is proportional to -ϕ^o at large time and increases slowly in time as seen in Fig. 2. The conditioned average of $\vartheta(\tau)$ is approximated by

$$\langle\vartheta(\tau)\rangle_{\varphi^0} = -\varphi^0\left(1+\frac{1}{\lambda_1^2}+\frac{1}{\lambda_2^2}\right)\left(1-F_m(\tau)\right), \quad (7)$$

where F_m is the memory function (with τ_m the memory characteristic time)

$$F_m(\tau) = \exp\left(-\frac{\tau}{\tau_m}\right). \quad (8)$$

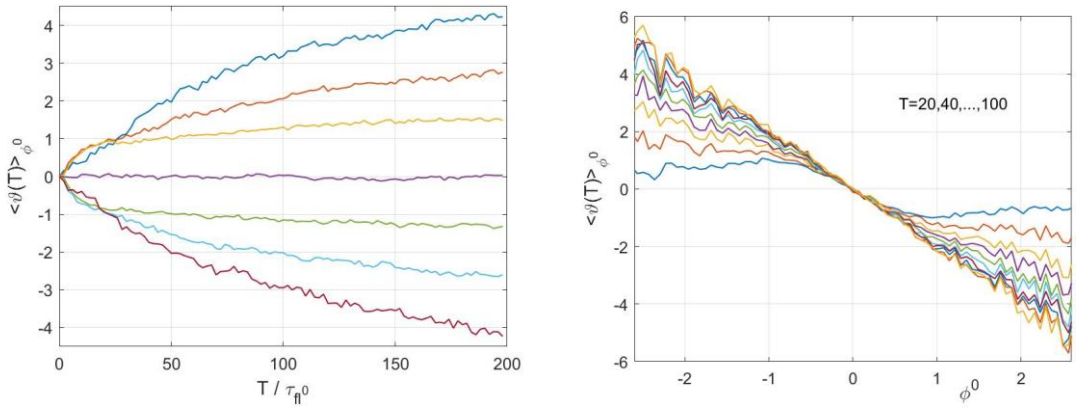

Figure 2 The conditioned average of the potential vorticity represented as function of time for several values of φ^0 (left panel) and as function of φ^0 for the time moments 20, 40, … (right panel)

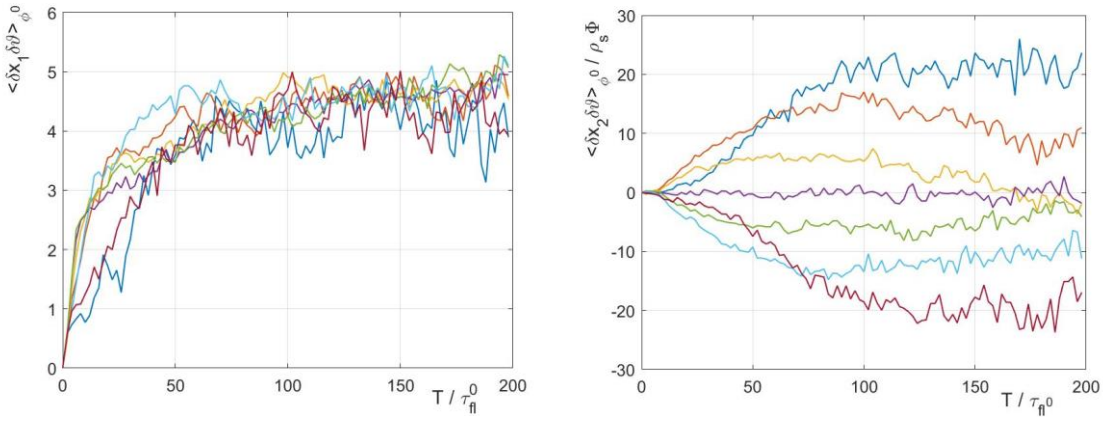

Figure 3 The conditional correlation of the displacements with the potential vorticity as function of time for the radial (left panel) and poloidal directions (right panel)

The correlations of $\vartheta(T)$ with the displacements are shown in Fig. 3. In the radial direction (left panel) it is positive with weak dependence on the initial potential, and saturates at a value of the order 4.5 in the case presented. The correlation with the poloidal displacements is anti-symmetric in ϕ^o at any time, and it has the sign of ϕ^o, as seen in Fig. 3 (right panel). It has a slow time evolution with a

maximum around T=100. All these quantities evolve at the large time scale of the memory.

The dispersion relation

$$-\left(k_y V_{*e} - \omega\rho_s^2 k_\perp^2\right)\bar{\Pi}_1^i - \bar{\Pi}_2^i = 1 + i\sqrt{\frac{\pi}{2}}\frac{\omega - k_y V_{*e}}{|k_z| v_{Te}}, \tag{9}$$

yields in dimensionless quantities

$$-\left(k_y - \omega k_\perp^2 + i k_i k_j D_{ij}\right)(I_1 + I_2) - \left(k_1\langle v_{1b}(\tau)\rangle_+ + \frac{1}{2}k_1 k_1 D_{12+}\right)(I_1 - I_2) - k_2 \mathrm{V}_2\left(I_1^\Delta + I_1^\Delta - I_1 + I_2\right) =$$

$$= 1 + i\sqrt{\frac{\pi}{2}}\frac{\omega - k_y V_{*e}}{|k_z| v_{Te}}, \tag{10}$$

where I_i and I_i^Δ are parts of the propagators. They are rather complicated functions of the 8 statistical quantities discussed above and in the previous report.

The solution has to be numerically obtained. This permits developments of the theoretical estimates and also eliminates the simplifications necessary in analytical solutions.

Test particle module

The test particle module is based on the codes developed in our group. The basic code for test particles in incompressible 2-dimensional velocity fields is used here.

The statistical quantities conditioned by the initial potential are determined. The domain of the potential φ^0 is divided in cells and the trajectories are attributed to each cell. The conditional averages of the displacements are determined for each cell. These are the averages and the mean square displacements

$$\langle x_1(t) - x_1\rangle_{\varphi^0}, \qquad \langle x_2(t) - x_2\rangle_{\varphi^0}, \qquad \langle \delta {x_1}^2(t)\rangle_{\varphi^0}, \qquad \langle \delta {x_2}^2(t)\rangle_{\varphi^0}, \qquad \langle \delta x_1(t)\, \delta x_2(t)\rangle_{\varphi^0},$$

and the average of the potential vorticity and its correlation with the displacements

$$\langle \vartheta(\mathrm{t})\rangle_{\varphi^0}, \qquad \langle \delta\vartheta(\mathrm{t})(x_1(t) - x_1)\rangle_{\varphi^0}, \qquad \langle \delta\vartheta(\mathrm{t})(x_2(t) - x_2)\rangle_{\varphi^0}.$$

The output of the test particle module consists, in principle, of 8 two-dimensional matrices that represent these statistical quantities as functions of φ^0 and t. A strong simplification consists in deriving simple analytical approximations from typical cases. Then, during the evolution of the spectrum of the turbulence, at each time step, the parameters of the approximations are determined by fitting procedures. This allows analytic estimations of the integrals over φ^0 and t in the propagators, which provide the dispersion relation (10). In particular, the characteristic time of memory τ_m can be determined

We underline that the long memory of the statistics of test particles leads to time dependent coefficients in the dispersion relation, which determine time variation of the growth rates and frequencies of the modes at the scale of τ_m.

Evolution of the spectrum

First results were obtained. They have to be analyzed and verified before a systematic study of the effects of the coherent ion motion on the evolution of turbulence.

We present here two examples:

- Run 1 is for a small density gradient, which determine a weak drive of the unstable drift modes. The ion trajectories are dominated by the random aspects and the coherence is weak.
- Run 2 is for a larger density gradient, which generates drift turbulence with significantly larger amplitude of the turbulence. The coherent components of ion motion are significant, but not dominant.

The evolution of the turbulence spectra in these runs is shown in Fig. 4. A smooth time dependence is observed in the Run 1 (upper panels), while the Run 2 is characterized by transitory acceleration and change of the shape of spectrum. This type of differences also appear in the Eulerian correlation of the potential (Fig. 5).

The evolution of the parameters of the turbulence is presented in Fig 6, where the upper panels are for Run 1 and the lower panels for Run 2. In the first case the fast initial growth of the amplitude of the turbulence is strongly reduced when the parameter K_* reaches the value 1, which corresponds to the lower limit of the nonlinear regime $K_* > 1$ (left panel). A faster decay of the dominant wave number and of the width of the spectrum appears from this moment t=12 (right panel). In the Run 2, the amplitude of the turbulence reaches much larger values, which correspond to $K_* \gg 1$, the nonlinear effects are stronger, and zonal flows are generated as a result of the hidden drifts.

The development of the spectrum of the zonal flows is shown in Fig. 7, left panel. It appears to be a complex process that is far from the smooth evolution in the quasilinear conditions (Fig. 4, upper panels). The generation of zonal flows appear to be associated to ion trapping in potential cells that are elongated in the radial direction (right panel).

A supplementary insight of the complex processes that appear in the Run 2 is suggested by Fig. 8, which shows that the turbulence oscillates behavior the linear and nonlinear regimes.

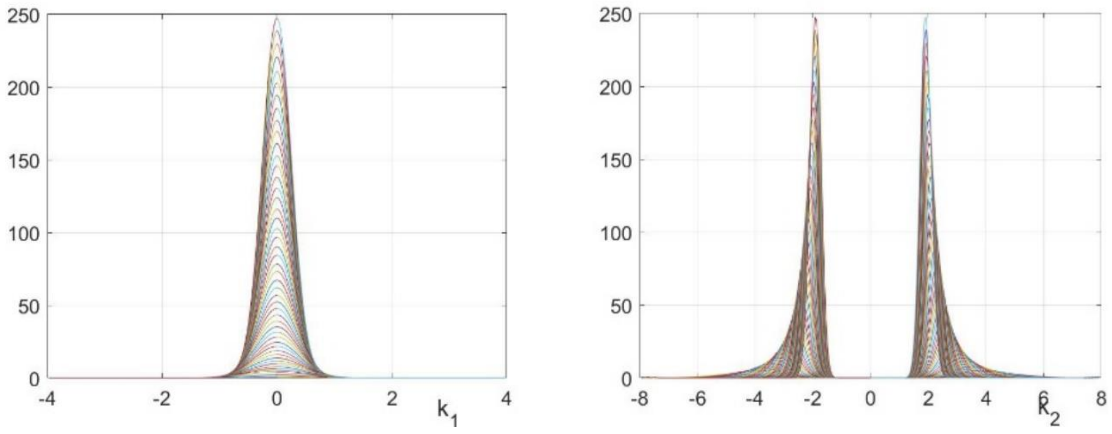

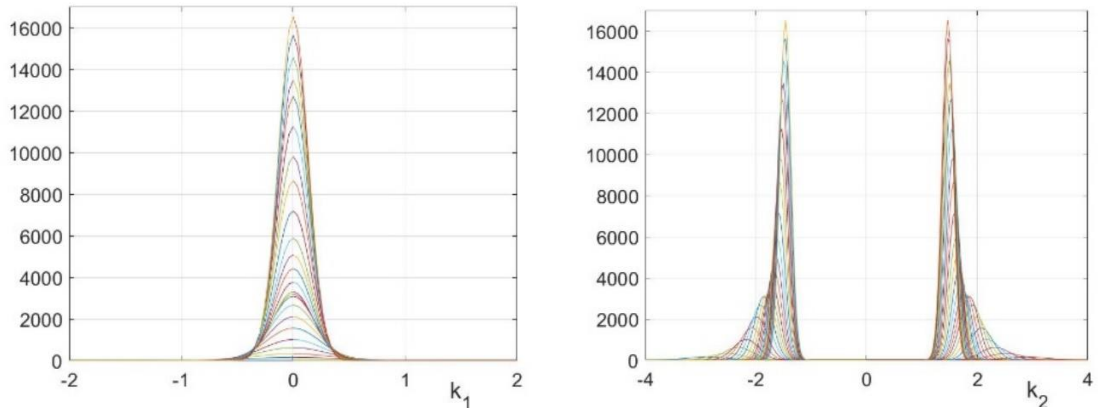

Fig. 4. Evolution of the turbulence spectra for the radial (left column) and poloidal (right column) wave numbers. Upper panels are for Run 1 and lower panels for Run 2.

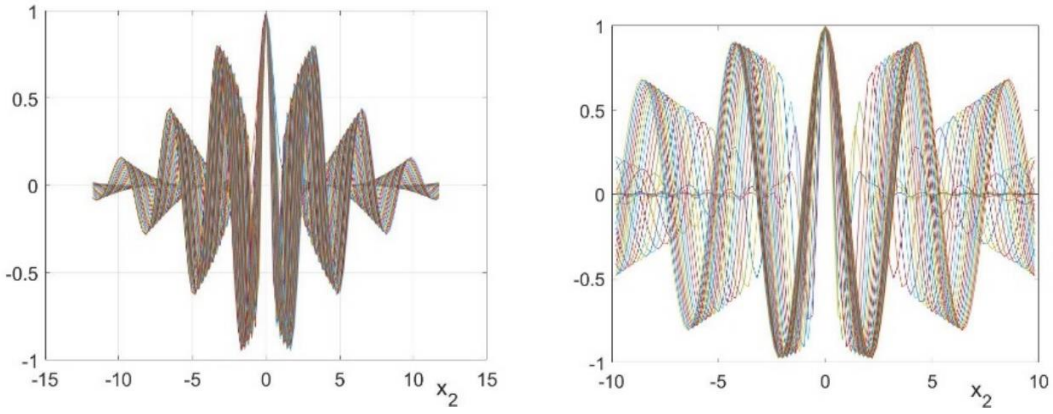

Figure 5. The Eulerian correlation of the potential along the poloidal direction obtained in Run 1 (left panel) and in Run 2 (right panel).

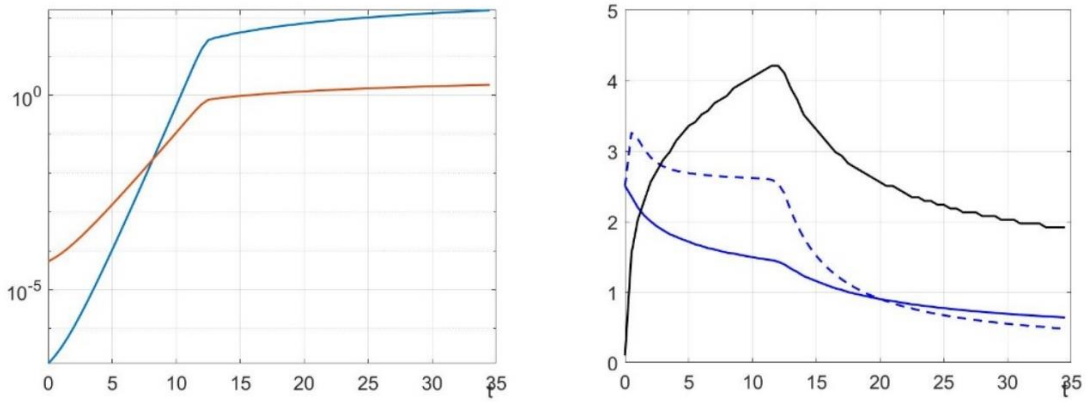

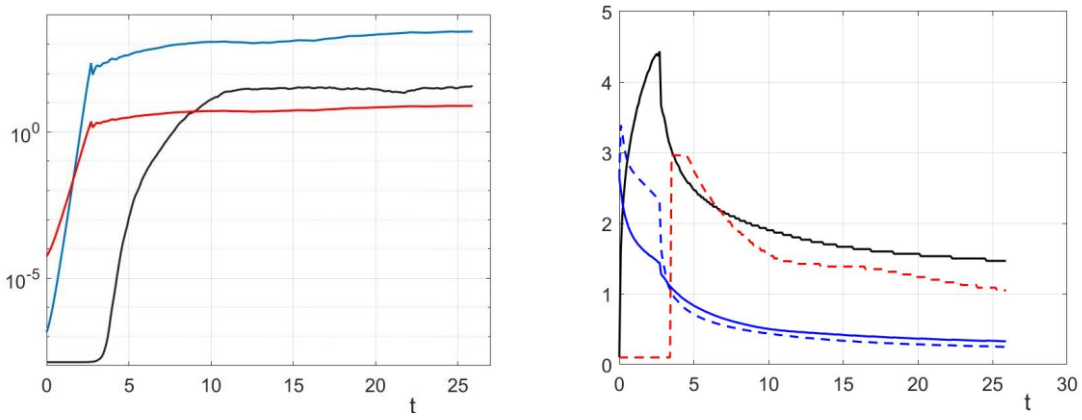

Figure 6. The upper panels are for Run 1 and the lower ones for Run 2.
Left: Time evolution of the amplitude of the turbulence Φ^2 (blue) and of the parameter K_* (red).
Right: The dominant wave number $k_{2,0}$ (black), the widths of the spectrum Δk_1 (dashed blue) and Δk_2 (blue).
Also shown are the characteristics of the zonal flow modes: the amplitude (red line, lower, left panel) and the dominant wave number $k_{1,zfm}$ (red line, lower, right panel)

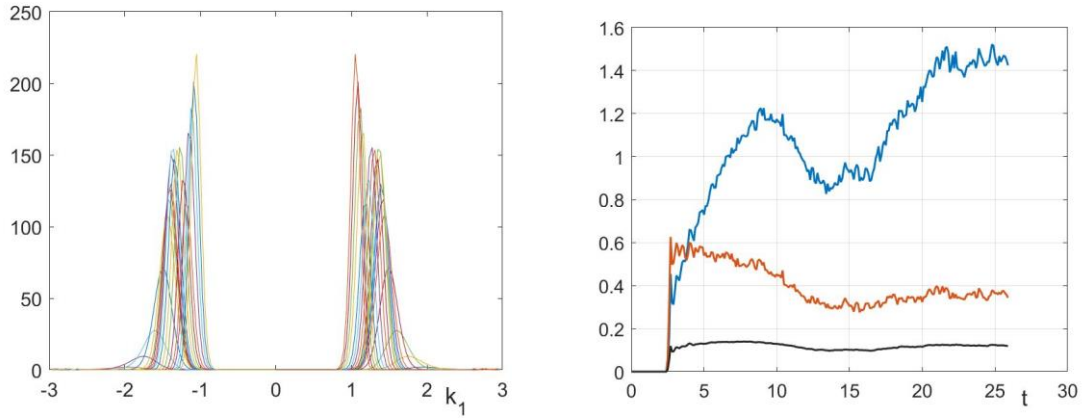

Figure 7 Left: The spectrum of the zonal flows. Right: the characteristics of the trapping process, the fraction of trapped ions (black), the size of the island of closed contour lines of the potential in the radial (blue) and poloidal (red) directions.

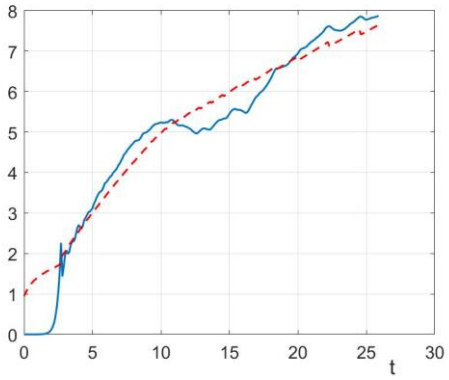

Figure 8. The time evolution of the parameter $K_*{}'$ (blue) and of the radial correlation length λ_1 (red) show oscillations between the linear ($K_*' < \lambda_1$) and the nonlinear ($K_*' > \lambda_1$) regimes.

B. *Database of simulations for the analysis of the experimental results on fluctuations and turbulent transport.*

New improvements to the numerical code for turbulent transport

The existing code dedicated to numerical investigations of turbulent transport is named "*T3ST*". In this stage of the project, the code has been upgraded to include several new capabilities. The two most significant enhancements in the latest version are: the inclusion of realistic magnetic equilibria and realistic collisions.

The realistic magnetic equilibrium surpasses the previous circular model implementation and accurately represents magnetic quantities as follows. The total magnetic field is considered axisymmetric in a covariant and contravariant representation:

$$\boldsymbol{B} = F(\psi)\nabla\zeta + \nabla\zeta \times \nabla\psi$$

Where $F(\psi)$ is an arbitrary function of the poloidal flux function ψ. The latter is axysymetrical $\psi \equiv \psi(R,Z) \equiv \psi(r,\theta)$. The standard cylindrical and toroidal coordinate systems, $(R,Z,\zeta),(r,\theta,\zeta)$ have been considered. Both coordinate systems are right-handed and orthogonal. The poloidal function $\psi(R,Z) = \psi(r,\theta)$ is a solution of the Grad-Shafranov equation:

$$\frac{\partial^2\psi}{\partial R^2} - \frac{1}{R}\frac{\partial\psi}{\partial R} + \frac{\partial^2\psi}{\partial Z^2} = -\mu_0 R^2\frac{dp}{d\psi} - \frac{1}{2}\frac{dF^2}{d\psi}.$$

Note that, in the neoclassical theory, both the pressure $p(\psi)$ and $F(\psi)$ are functions of poloidal flux. Consequently, one can define the function

$$q_\theta = \frac{B\cdot\nabla\zeta}{B\cdot\nabla\theta}$$

The safety factor is

$$\bar{q}(\psi) = \frac{1}{2\pi}\int_0^{2\pi} q_\theta(\psi,\theta)d\theta$$

And the generalized poloidal angle:

$$\frac{\partial\chi}{\partial\theta} = \frac{q_\theta(\psi,\theta)}{\bar{q}(\psi)}.$$

As a result of these definitions, all magnetic quantities related to MHD equilibrium, which appear explicitly in the equations of motion of gyro-centers, can be expressed in terms of $\psi(R,Z)$ and its derivatives. This allows us to use realistic magnetic equilibrium data from tokamak experiments, provided in the so-called G_EQDSK files. Combined with an interpolation approach, this leads to an accurate evaluation of all magnetic drifts. Moreover, field-aligned coordinates (x,y,z) used for turbulence representation are also readily computable as follows:

$$x = C_x(\psi - \psi_0)$$

$$y = C_y(\zeta - \bar{q}\chi)$$

$$z = C_z\chi$$

The turbulent fields are computed as:

$$\phi(\boldsymbol{r},t) = \phi(x,y,z,t) = \int d\boldsymbol{k}^3\, \tilde{\phi}(\boldsymbol{k}) e^{i(\boldsymbol{kr}-\omega_{\boldsymbol{k}}t)} = \int d\boldsymbol{k}^3\, S^{\frac{1}{2}}(\boldsymbol{k})\zeta(\boldsymbol{k}) e^{i(\boldsymbol{kr}-\omega_{\boldsymbol{k}}t)}$$

Where, $V_\star = \nabla T_i \times \frac{b}{qnB}$, $k_\perp^2 = \left(\boldsymbol{k} - \boldsymbol{b}(\boldsymbol{k}\cdot\boldsymbol{b})\right)^2$ and

$$\omega_k = \frac{T_i}{T_e}\frac{\boldsymbol{k}\cdot\boldsymbol{V}_\star}{1+\rho_s^2 k_\perp^2}$$

Without detailing the numerical implementation, we extract here in Fig 1 two snapshots of the routines dedicated to the interpolation of G_EQDSK data to particle positions (EFITsa) and to the evaluation of magnetic drift quantities (Equlibrium_magn).

```
  SUBROUTINE EFITsa(X,Y,R)
  USE constants
  IMPLICIT NONE

    ! I/O variables
  REAL(KIND = dp),  DIMENSION(Np),          INTENT(IN)   :: X, Y
  REAL(KIND = dp),  DIMENSION(Nqua,Np),     INTENT(OUT)  :: R

    ! Local variables
  INTEGER,  DIMENSION(Np)                                :: poz1, poz2, poz
  INTEGER                                                :: i,j,k
  REAL(KIND = dp),  DIMENSION(Np)                        :: F1, F2, F3, F4, X1,Y1,Xef,Yef
  REAL(KIND = dp),  DIMENSION(Np)                        :: rr, theta, chi, chir, chiz

  poz1 = modulo(int((X - minR)/stepR),NgridR)
  poz2 = modulo(int((Y - minZ)/stepZ),NgridZ)
  X1 = minR + poz1*stepR
  Y1 = minZ + poz2*stepZ
  Xef = (X - X1)/stepR
  Yef = (Y - Y1)/stepZ

DO i=1,Nqua-3
    DO j=1,Np

       F1(j) = Efit_data(NgridR*NgridZ*(i-1) + poz1(j)*NgridR + poz2(j))
       F2(j) = Efit_data(NgridR*NgridZ*(i-1) + (poz1(j)+1)*NgridR + poz2(j))
       F3(j) = Efit_data(NgridR*NgridZ*(i-1) + poz1(j)*NgridR  + poz2(j) + 1)
       F4(j) = Efit_data(NgridR*NgridZ*(i-1) + (poz1(j)+1)*NgridR + poz2(j)+1)
    END DO
       R(i,:) = F1 + (F2-F1)*Xef + (F3-F1)*Yef + Xef*Yef*(F1+F4-F2-F3)
END DO


   rr = sqrt((X - 1.0)**2 + Y**2) + 0.0000001
   theta = atan2(Y, X-1.0)       ! atan(z,rr)
   chi = 2.0*atan(sqrt((1.0-rr)/(1.0+rr))*tan(theta/2.0))
   chir = sin(theta)*(rr**2 - X)/X/rr/Sqrt(1.0-rr**2)
   chiz = -(rr-cos(theta))/rr/Sqrt(1.0-rr**2)

   R(11,:) = chi
   R(12,:) = chir
   R(13,:) = chiz
```

```
! ------------------------------------------------------------------------------
! R contains: d_r\psi, d_z\psi, F(psi), rot(b), grad(B)
! ------------------------------------------------------------------------------

   CALL MagnModel(X,Y,R)
   q1 = C1*(psi - psi0)
   q2 = C2*(Z - q00*chi)
   q3 = C3*chi

! ------------------------------------------------------------------------------
! Magnetic field components
! ------------------------------------------------------------------------------

Bx  = - psiz/X                                          ! covariant component of B on
By  =   psir/X                                          ! covariant component of B on
Bz  =   Fpsi/X**2                                       ! covariant component of B on

B = sqrt(Bx**2*hx**2 + By**2*hy**2 + Bz**2*hz**2)       ! the norm of the magnetic fie

! ------------------------------------------------------------------------------
! Gradients and curls
! ------------------------------------------------------------------------------

gradBx = - (Fpsi**2*psir**2+psiz**2-Fpsi*Fprim*X*psir - X*psir*psirr - psiz*X*psirz)/B/X**3
gradBy = (Fpsi*Fprim*psiz + psir*psirz + psiz*psizz)/B/X**2   ! grad B proj. on x
gradBz = 0.0                                                  ! grad B proj. on x

rotbx = (Fprim*psiz*(psir**2+psiz**2) - Fpsi*(psir*psirz + psiz*psizz))/B**3/X**3
rotby = - (Fpsi**3 + Fpsi*(psir**2+psiz**2) - X*Fpsi*(psirz*psiz+psir*psirr) + X*Fprim*psir*
rotbz = - (Fpsi*Fprim*(psir**2+psiz**2) - Fpsi**2*(psir**2+psiz**2) - &
&psirr*psiz*psiz - psizz*psir*psir + 2.0*psirz*psir*psiz)/B**3/X**4  ! curl of u proj on z

rotux = Omgt0*(-X*psiz*Omgtprim)                              ! curl of u proj on x
rotuy = Omgt0*(2.0 + X*psir*Omgtprim)                         ! curl of u proj on y
rotuz = 0.0                                                   ! curl of u proj on z

gradu2x = Omgt0**2*X*(1.0 + X*psir*Omgtprim)                  ! grad u**2 proj. on x
gradu2y = Omgt0**2*X**2*psiz*Omgtprim                         ! grad u**2 proj. on y
gradu2z = 0.0                                                 ! grad u**2 proj. on z
```

Fig.1 Snapshots of EFITsa and Equlibrium_magn Fortran routines dedicated to the evaluation of magnetic quantities along test-particle positions using (or not) G_EQDSK reconstructions of equilibria.

Regarding the implementation of collisions, we have used a theoretical description of how collisions impact the individual gyrocenters in a Monte-Carlo framework. While the equations involved are quite intricate, we offer here only a snapshot of the Fortran routine dedicated to collisions (Fig. 2).

```
[hx,hy,hz] = [1.0,1.0,X]

[betx,bety,betz] = [Bx*hx/B, By*hy/B,Bz*hz/B]
Omega= B/Aw*wi*R0/vth

ene  = Aw/2.0*Vp**2 + B*abs(mut)
v    = sqrt(2.0*abs(ene)/Aw)
zeta = Vp/v
alf  = ene/(v*B)
xx   = v/sqrt(2.0)/Sqrt(Aeff)
Fphi = erf(xx)
Fpsi = (Fphi-2.0*xx*exp(-xx**2)/sqrt(pi))/2.0/xx**2

Dpar  = 4.0*R0*c0/vth**4*sqrt(Aeff/2.0)*Fpsi/xx
Dperp = 2.0*R0*c0/vth**4*sqrt(Aeff/2.0)*(Fphi - Fpsi)
Dparprim = - Dpar*((6.0*xx + 4.0*xx**3)*exp(-xx**2) - 3.0*Sqrt(Pi)*Erf(xx))/(xx*((2.0*xx)*exp(-xx**2) - Sqrt(Pi)*Erf(xx)))
DifR = (Dpar*(1.0-zeta**2) + Dperp*(1.0+zeta**2))/2.0/Omega**2
nuf = 4.0*R0*c0/vth**4*(sqrt(Aeff/2.0)**3)*Fpsi!!

CALL PDF_G(5,Np,grf(1:5,:))           ! corr = 1 ~ (PDF_G, PDF_G, PDF_w_Bes)

Wm = grf(1,:)/sqrt(dt)
Wp = grf(2,:)/sqrt(dt)
Wx = grf(3,:)/sqrt(dt)
Wy = grf(4,:)/sqrt(dt)
Wz = grf(5,:)/sqrt(dt)

Spp = Sqrt(Dpar*zeta**2 + Dperp*(1.0 - zeta**2)) + 0.000001
Spm = 0.0
Smp = 2.0*Sqrt(2.0)*alf*zeta*(Dpar - Dperp)*(1.0 - zeta**2)/Spp
Smm = 2.0*Sqrt(2.0)*alf*Sqrt(Dpar*Dperp*abs(1.0 - zeta**2))/Spp
Spp = Sqrt(2.0)*Spp

vcolp = (- nuf*Vp + zeta*(2.0*(Dpar-Dperp)/v + Dparprim))*1.0 + 1.0*(Spp*Wp + Spm*Wm)
vcolm = (- 2.0*nuf*mut + Aw*mut/ene*(v*Dparprim + 3.0*(Dpar-Dperp)) + 2.0*Aw*Dperp/B)*1.0 + 1.0*(Smp*Wp + Smm*Wm)
vcolx = sqrt(2.0*DifR)*(Wx - Wx*betx*betx - Wy*bety*betx - Wz*betz*betx)/hx
vcoly = sqrt(2.0*DifR)*(Wy - Wx*betx*bety - Wy*bety*bety - Wz*betz*bety)/hy
vcolz = sqrt(2.0*DifR)*(Wz - Wx*betx*betz - Wv*betv*betz - Wz*betz*betz)/hz
```

Fig.2. Snapshot of the "Collisions" routine dedicated to the evaluation of test-particle motion due to collisions with the ionic background

Numerical tests of the code

One of the fundamental features of particle dynamics in tokamak environments is that, in the absence of collisions or turbulence, trajectories are closed, either as circulating or as banana orbits. Therefore, this topological behaviour should be observed for individual particles in our numerical simulations and serves as a minimal test for the correct implementation of the neoclassical part of drifts.

In Fig. 3, we plot the results of two distinct trajectories obtained in an MHD equilibrium corresponding to a numerical reconstruction of the WEST tokamak. As shown, we recover both behaviours of circulating (blue) and banana (orange) paths.

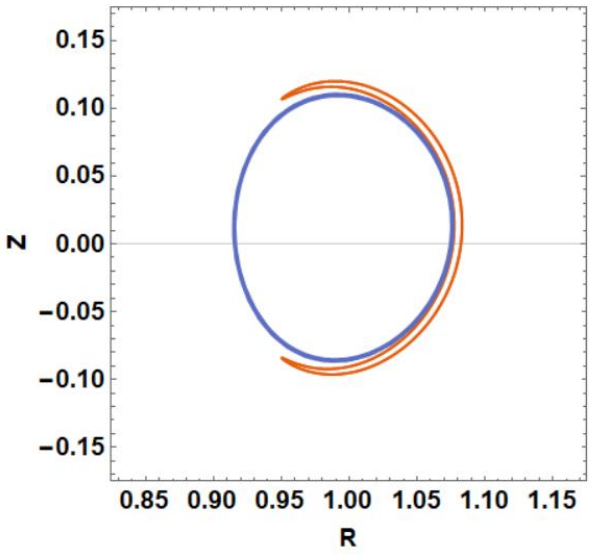

Fig.3. Typical circulating (blue) and trapped (banana, orange) neoclassical trajectories in a realistic MHD equilibrium corresponding to the WEST tokamak.

Unfortunately, this is merely a qualitative test and does not constitute a complete verification of our code. For comprehensive validation, we must conduct quantitative tests. The fact that particle trajectories have such closed, special topologies is intimately related to the conservation of certain invariants of motion, one of which is energy.

$$H = \frac{mv_{\parallel}^2}{2} - \frac{mu^2}{2} + \mu B + q\Phi$$

For this reason, we test the code's ability to conserve the Hamiltonian for pure neoclassical trajectories. We find that the RK4 algorithm, in conjunction with appropriate time steps, offers a high degree of conservation. It is important to note that collisions were set to zero to preserve the Hamiltonian.

The results are shown in Fig. 4, displaying both the evolution of multiple relative energies and the numerical dispersion of the invariant at the end of the computation time. We conclude that conservation is very well reproduced, with errors lying in the range of approximately 0.1 ‰.

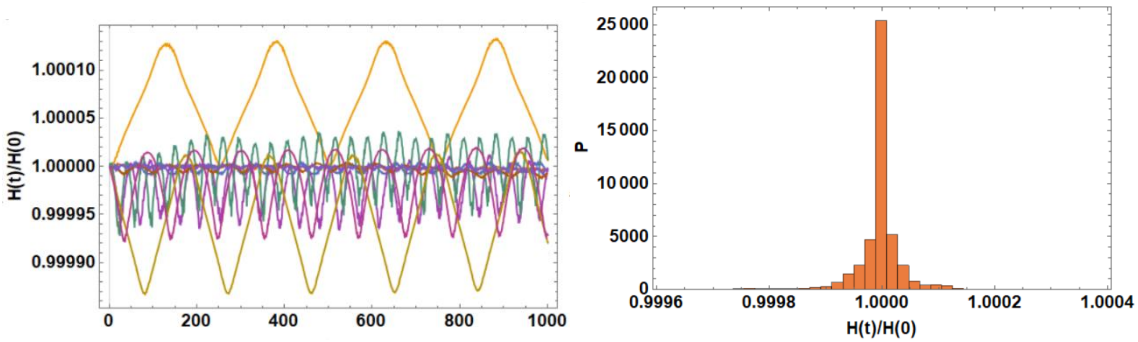

Fig.4. a) Time evolution of the energy $H(t)$ relative to its initial value $H(t=0)$ for multiple neoclassical trajectories. b) Distribution of relative energies at the end of computing time for a simulation of neoclassical dynamics. Note that all results are in the absence of collisions.

Adding turbulence into the picture leads to perturbed trajectories that, in general, no longer conserve energy. However, there is a special case where this invariance is still maintained: frozen turbulence. While this is an idealization that is not particularly relevant to tokamak plasmas, it serves as a robust test of the code. Testing the conservation of a quantity in both pure neoclassical regimes and in neoclassical plus turbulence regimes offers an effective method to isolate possible deviations from the desired results.

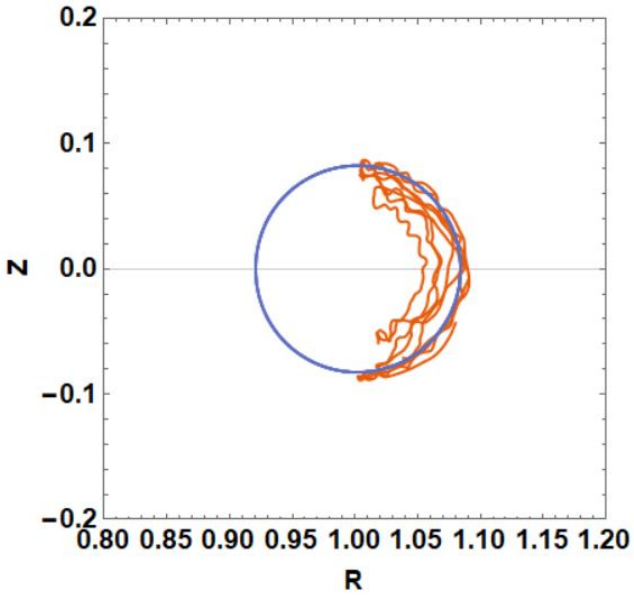

Fig.3. Typical circulating (blue) neoclassical trajectories and the same trajectory in the presence of turbulence (orange). The circular model was used to reduce interpolation errors.

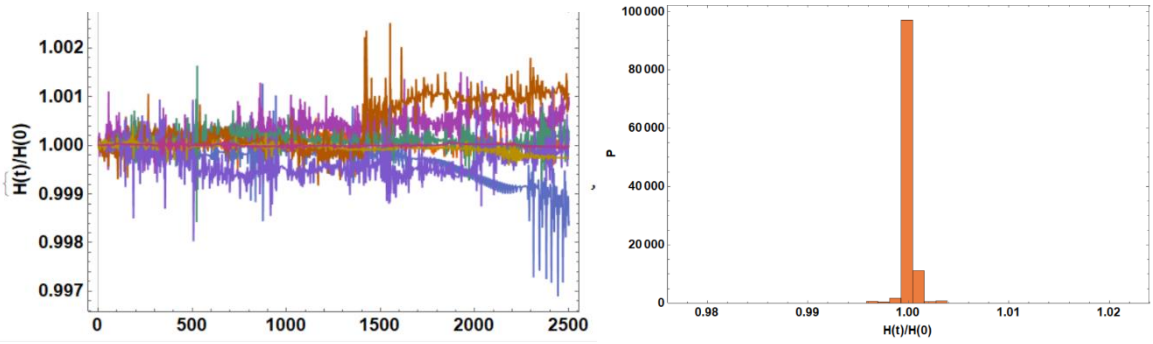

Fig.6. a) Time evolution of the energy $H(t)$ relative to its initial value $H(t=0)$ for multiple turbulent trajectories. b) Distribution of relative energies at the end of computing time for a simulation of turbulent dynamics. Note that all results are in the absence of collisions.

Numerical results, analogous to the pure neoclassical motion, can be seen in Figs. 5 and 6. Fig. 5 depicts the effect of turbulence (orange) on a purely circulating trajectory (blue), leading to the trapping effect. In Fig. 6, we observe how propagating particles in frozen turbulence induce small numerical oscillations in the relative energy, which are almost two orders of magnitude larger than in the neoclassical case.

However, these oscillations still successfully reproduce invariants, as the energy error fluctuation remains around ~0.1%.

A much more complex test for the code involves quantities that are not solely related to individual trajectories but rather to global transport, specifically the transport coefficients. Unfortunately, analytical data in this regard is quite scarce. Nonetheless, we rely on one of the oldest results of neoclassical theory: the classification of transport regimes. Heuristic arguments, supported by drift-kinetic equations, show that neoclassical transport—resulting from collisions combined with magnetically confined motion—leads to diffusive transport. The associated coefficient strongly depends on a scaled version of the collisional frequency, $\nu^\star = \nu q R/v_{th}$. There are three distinct regimes: banana, plateau, and the Pfirsch-Schlüter regime. In the banana regime ($\nu^\star \ll 1$), diffusion follows $D \propto \epsilon^{3/2}\nu^\star$. In the plateau regime ($\nu^\star \sim 1$) , diffusion is approximately constant $D \approx const$. In the Pfirsch-Schlüter regime ($\nu^\star \gg 1$), diffusion again follows $D \propto \epsilon^{3/2}\nu^\star$. Our numerical simulations successfully reproduce this behavior, as shown in Fig. 7. To obtain these results, we artificially increased the collision rate ν experienced by ions to cover a large range of parametric values. It is worth noting that the Pfirsch-Schlüter regime is rarely relevant to tokamak discharges.

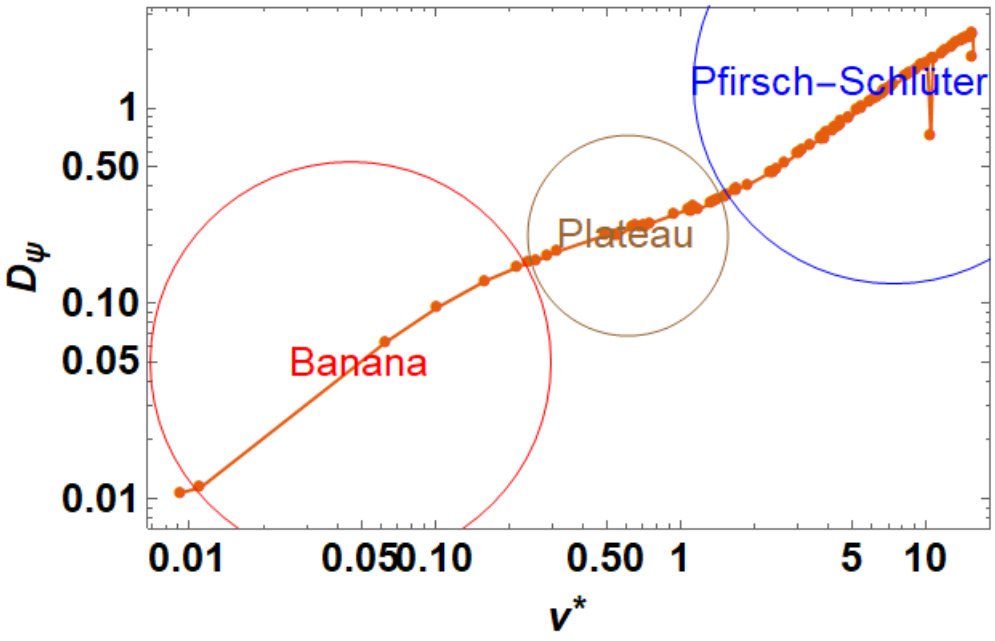

Fig 7. Banana, plateau and the Pfirsch-Schlüter regime reproduced sucesfully by our numerical simulations for the neoclassical transport (magnetic drifts + collisions).

The parametric space of the database

One of the objectives of the present project is to construct a database of simulations of transport. The purpose of this task is to quantify the relation between the characteristics of turbulent fluctuations and the associated transport. Furthermore, it is expected that, in the near future, such databases could be validated against theoretical and experimental results and used as means to diagnose both the transport and the turbulence in tokamak plasmas.

The full set of parameters that characterize a single simulations are 22 in number and can be seen in Table. 1. They cover both plasma equilibrium quantities (temperatures T_i, T_e, magnetic fields B_0, geometrical properties of the tokamak R_0, a, density n_0, etc.) as well as particle properties (mass, m, charge q, phase space distribution, temperature T) and turbulent features (amplitude Φ, correlation lengths $\lambda_x, \lambda_y, \lambda_z, \tau_c, k_0^i, k_0^e$).

Parameter	Interpretation	Reference value	Interval of variation
T_i	Ion temperature	$1\ keV$	$[0.1-4]keV$
T_e	Electron temperature	$1\ keV$	$[0.1-4]keV$
B_0	Magnetic field value near axis	$3.7\ T$	$[2-4]T$
R_0	Large radius	$2.5\ m$	$[2-4]m$
a	Small radius	$0.5\ m$	$[0.2-1]m$
n_0	Plasma density	$2\times10^{19}m^{-3}$	–
A	Mass number	1	$[1-10]$
Z	Charge number	1	$[1-10]$
T	Species temperature	$1\ T_i$	$[0-4]T_i$
q_1	Safety factor core value	1.5	$[0.5-2]$
q_3	Safety factor shear parameter	3.5	$[1-10]$
r_0	Radial position	0.2	$[0.05-0.35]$
Ω_t	Toroidal rotation	0	$[0-20]kHz$
Ω_p	Poloidal rotation	0	–
Z_{eff}	Effective ion charge	1	–
A_{eff}	Effective ion mass	1	–
P	Local plasma pressure	$40\ kPa$	$[10-100]kPa$
$P'(\psi)$	Local plasma pressure gradient	$-7\times10^4 Pa/(Tm^2)$	$-[10-100]kPa/m^2T$
Φ	Effective, local, turbulence amp.	1%	$[0-5]$%
λ_x	Radial correlation lenght	$5\rho_i$	$[1-10]\rho_i$
λ_y	Poloidal correlation lenght	$5\rho_i$	$[1-10]\rho_i$
λ_z	Parallel correlation lenght	$1R_0$	$[0.2-2]R_0$
τ_c	Correlation time	∞	$[10-100]R_0/v_{th}$
k_0^i	Dominant ITG mode no.	0.1	$[0.05-0.5]\rho_i^{-1}$
k_0^e	Dominant TEM mode no.	0.1	$[0.05-0.5]\rho_i^{-1}$

Table 1. Free parameters of the model to be varied individually within the database. On the first column is the denomination of each parameter, on the second its interpretation, on the third the baseline value while on the last, its interval of variation.

Clearly, our space is 22-dimensional. Even attempting 2 discrete points along each dimension results in $2^{22} \approx 10^7$ simulations, far exceeding our current computational capabilities. Moreover, employing just 2 points per dimension is insufficient; a minimum of 10 points per direction is necessary to achieve a baseline level of accuracy in our database. Given the impracticality of fully populating the database, we vary one parameter at a time around the baseline scenario to discern qualitative trends in transport relative to each specific parameter. Following this approach, we conducted 2200 simulations (100 per parameter), and the results are presented graphically (see Fig. 8).

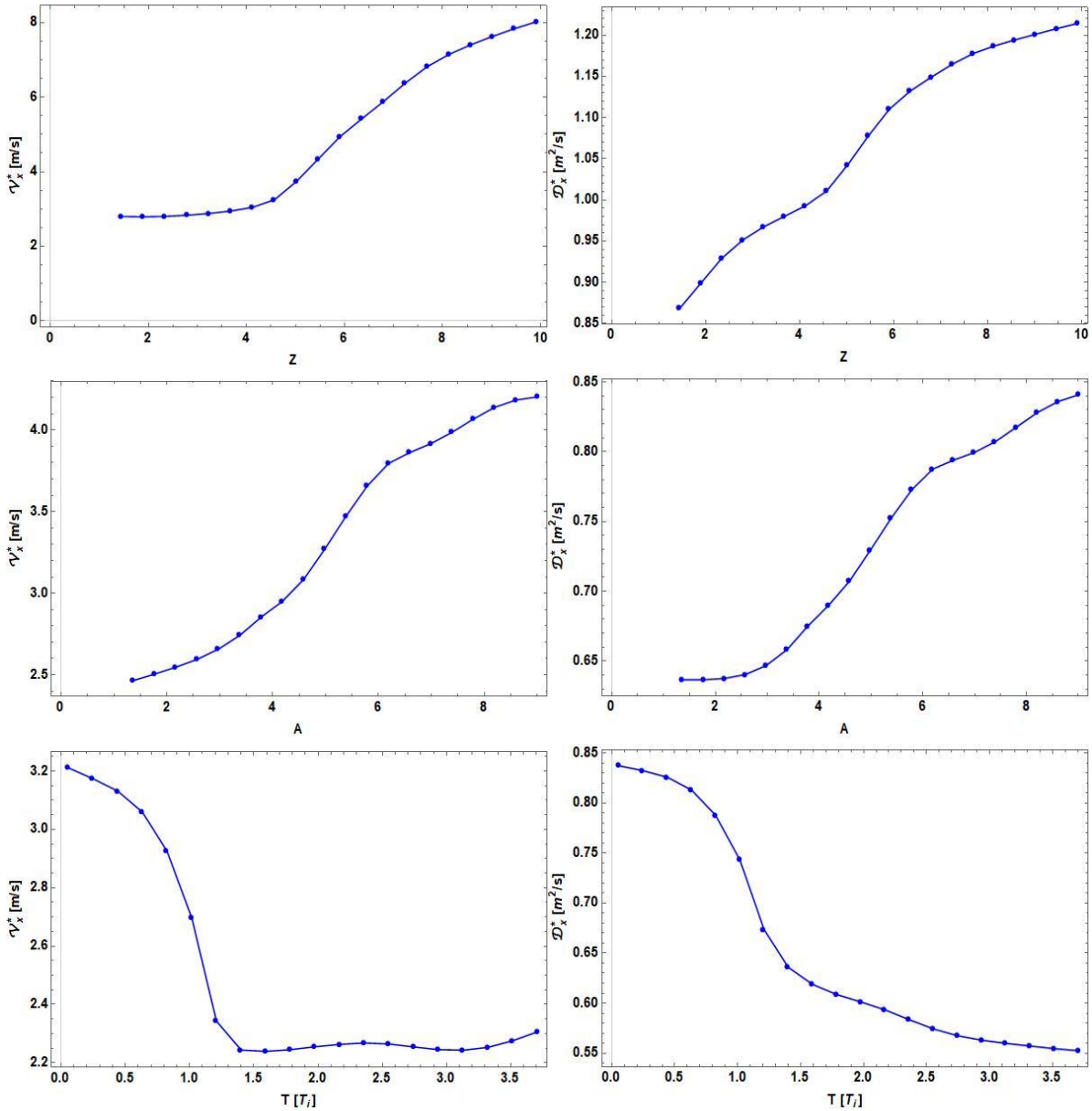

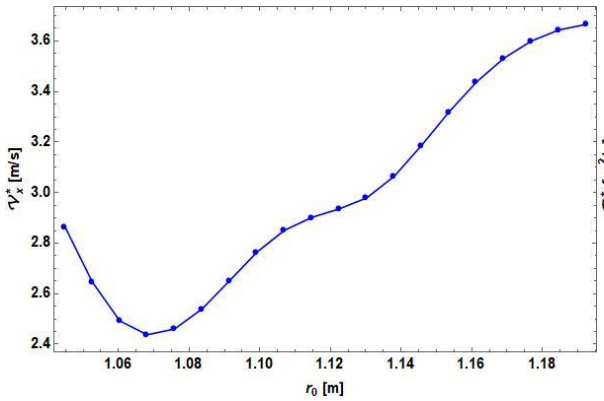
$\mathcal{V}_x^*$ [m/s]
r_0 [m]

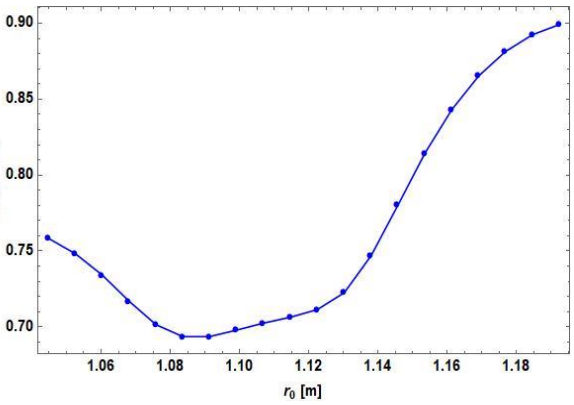
$\mathcal{D}_x^*$ [m^2/s]
r_0 [m]

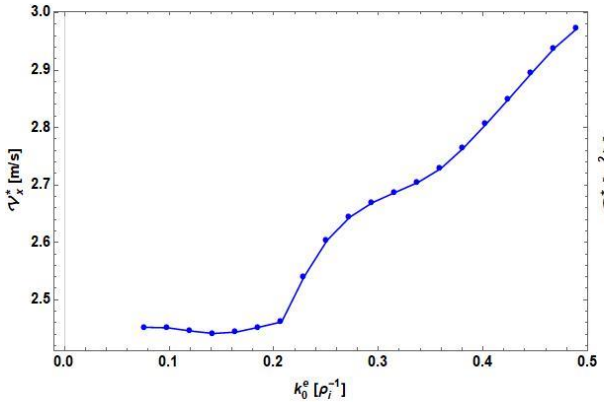
$\mathcal{V}_x^*$ [m/s]
k_0^e [ρ_i^{-1}]

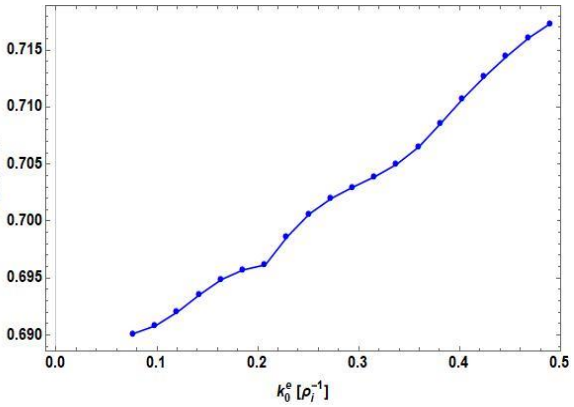
$\mathcal{D}_x^*$ [m^2/s]
k_0^e [ρ_i^{-1}]

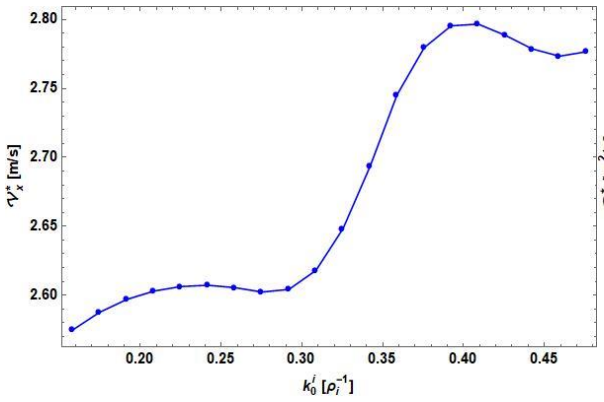
$\mathcal{V}_x^*$ [m/s]
k_0^i [ρ_i^{-1}]

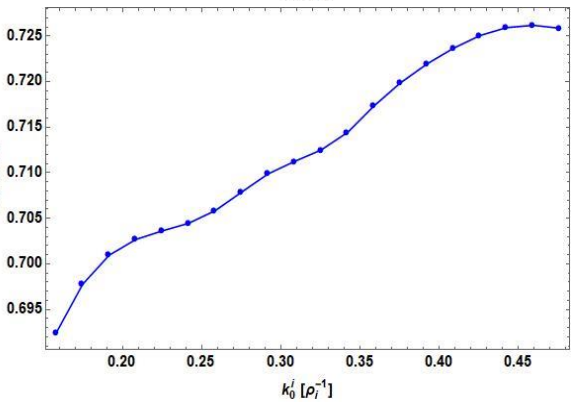
$\mathcal{D}_x^*$ [m^2/s]
k_0^i [ρ_i^{-1}]

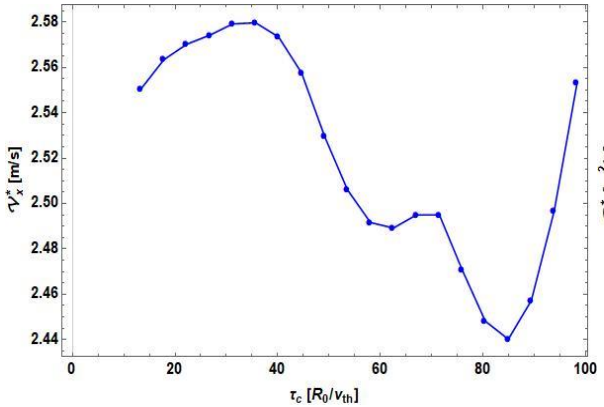
$\mathcal{V}_x^*$ [m/s]
τ_c [R_0/v_{th}]

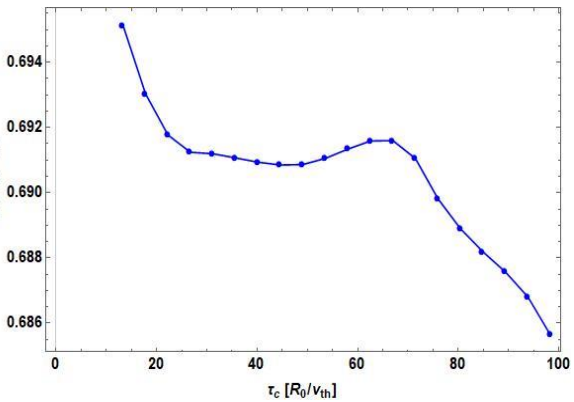
$\mathcal{D}_x^*$ [m^2/s]
τ_c [R_0/v_{th}]

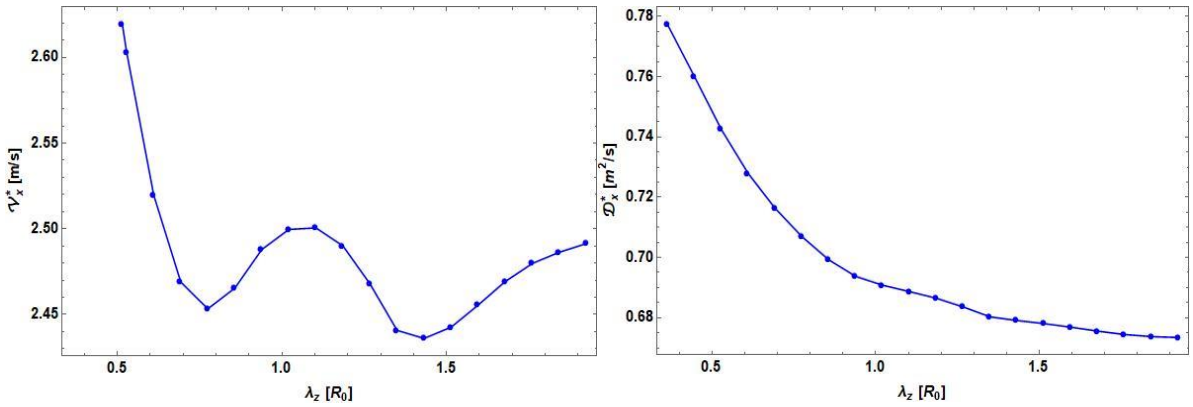
$\mathcal{V}_x^*$ [m/s]
2.60
2.55
2.50
2.45
0.5
1.0
1.5
λ_z [R_0]

$\mathcal{D}_x^*$ [m^2/s]
0.78
0.76
0.74
0.72
0.70
0.68
0.5
1.0
1.5
λ_z [R_0]

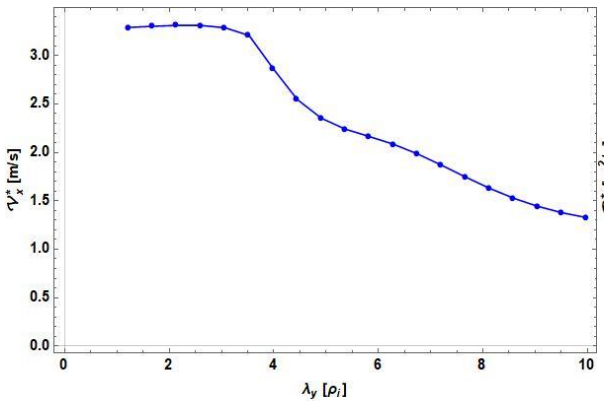
$\mathcal{V}_x^*$ [m/s]
3.0
2.5
2.0
1.5
1.0
0.5
0.0
0
2
4
6
8
10
λ_y [ρ_i]

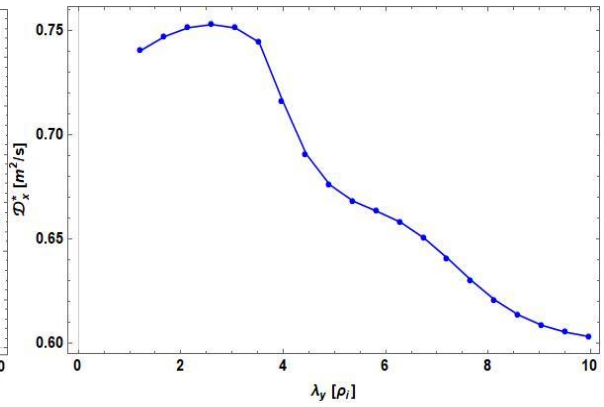
$\mathcal{D}_x^*$ [m^2/s]
0.75
0.70
0.65
0.60
0
2
4
6
8
10
λ_y [ρ_i]

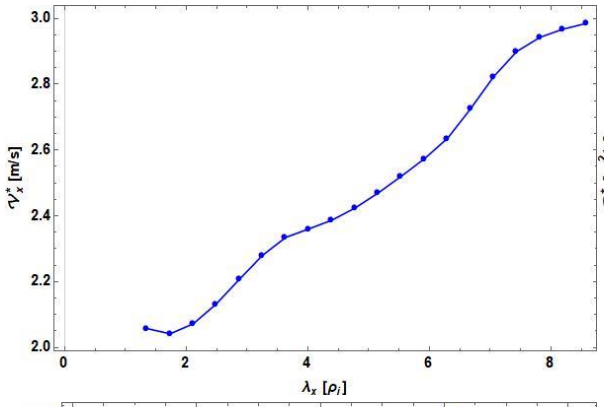
$\mathcal{V}_x^*$ [m/s]
3.0
2.8
2.6
2.4
2.2
2.0
0
2
4
6
8
λ_x [ρ_i]

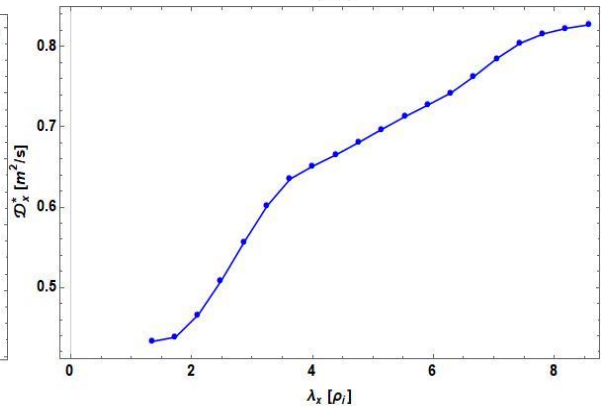
$\mathcal{D}_x^*$ [m^2/s]
0.8
0.7
0.6
0.5
0
2
4
6
8
λ_x [ρ_i]

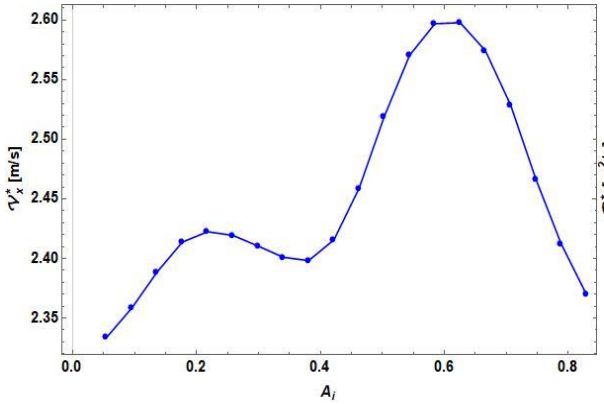
$\mathcal{V}_x^*$ [m/s]
2.60
2.55
2.50
2.45
2.40
2.35
0.0
0.2
0.4
0.6
0.8
A_i

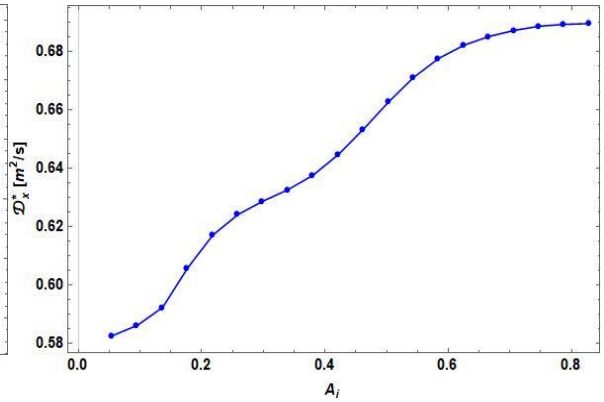
$\mathcal{D}_x^*$ [m^2/s]
0.68
0.66
0.64
0.62
0.60
0.58
0.0
0.2
0.4
0.6
0.8
A_i

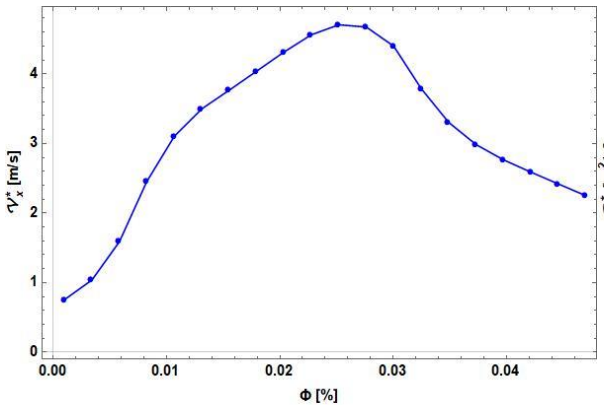
$\mathcal{V}_x^*$ [m/s]
Φ [%]

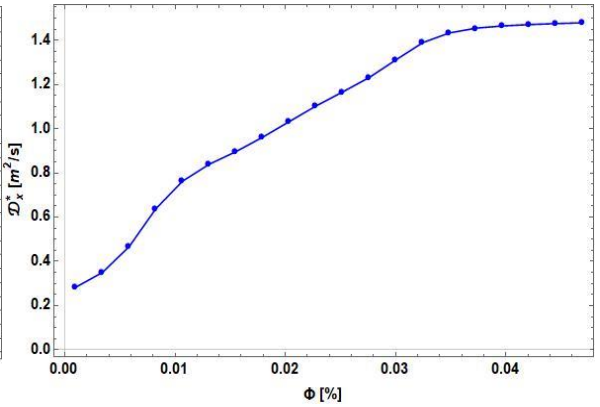
$\mathcal{D}_x^*$ [m^2/s]
Φ [%]

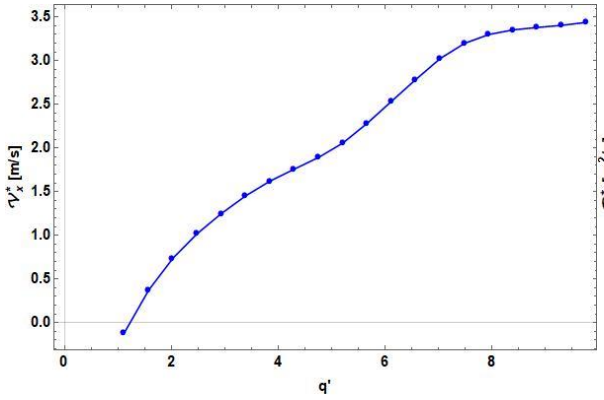
$\mathcal{V}_x^*$ [m/s]
q'

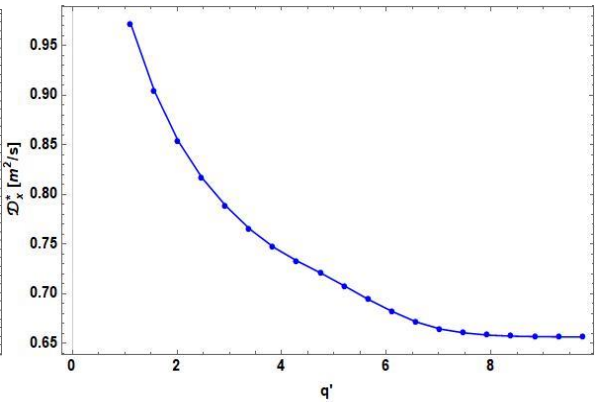
$\mathcal{D}_x^*$ [m^2/s]
q'

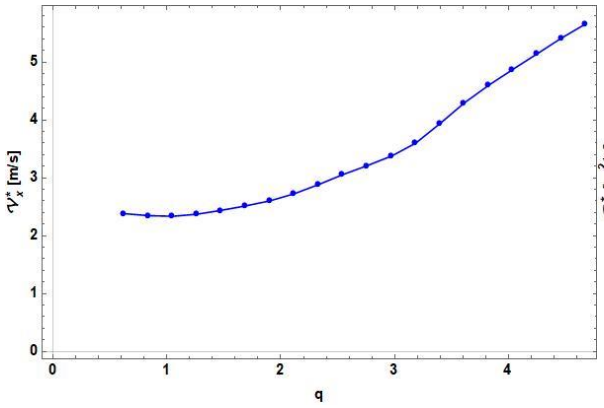
$\mathcal{V}_x^*$ [m/s]
q

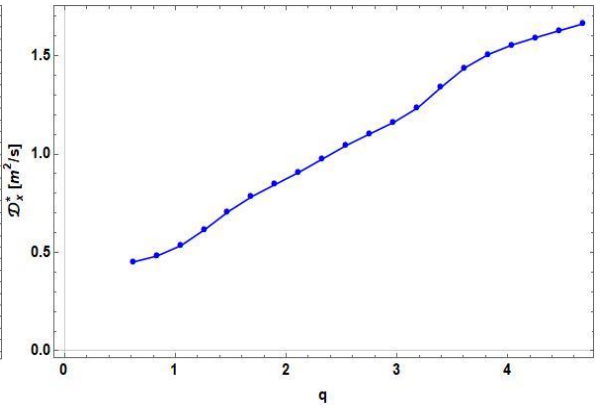
$\mathcal{D}_x^*$ [m^2/s]
q

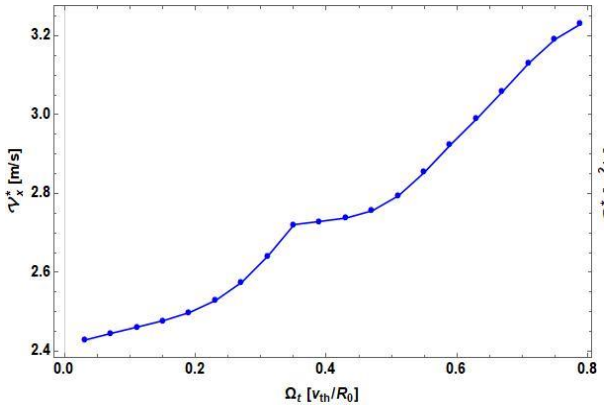
$\mathcal{V}_x^*$ [m/s]
Ω_t [v_{th}/R_0]

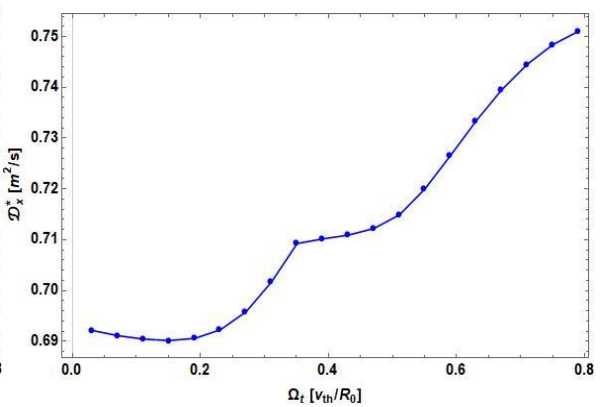
$\mathcal{D}_x^*$ [m^2/s]
Ω_t [v_{th}/R_0]

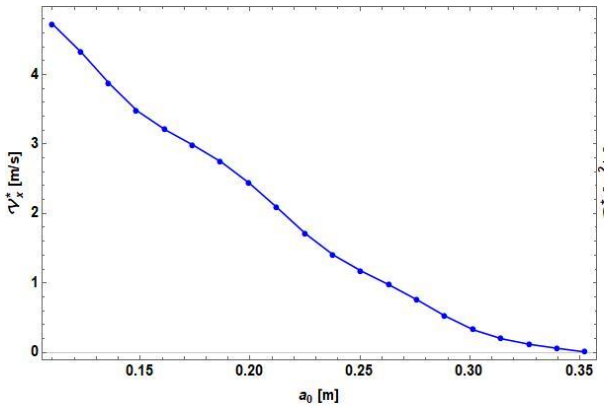
$\mathcal{V}_x^*$ [m/s]
a_0 [m]

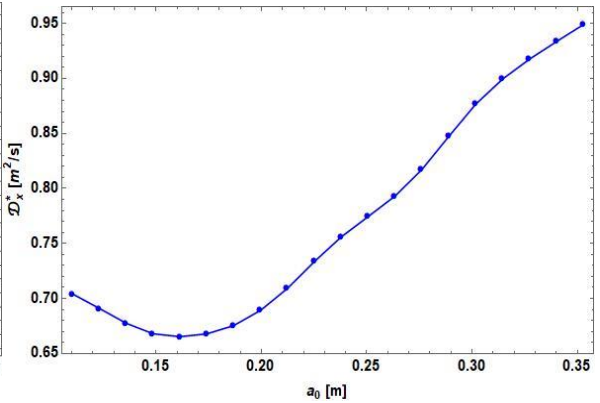
$\mathcal{D}_x^*$ [m^2/s]
a_0 [m]

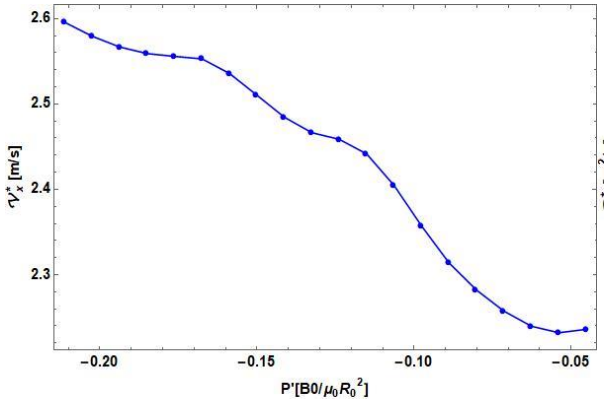
$\mathcal{V}_x^*$ [m/s]
P'[B0/$\mu_0 R_0^2$]

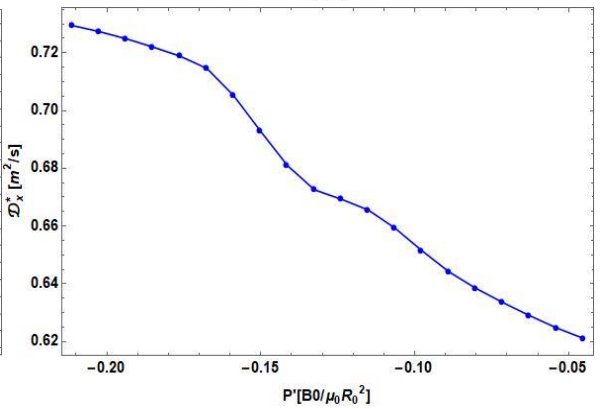
$\mathcal{D}_x^*$ [m^2/s]
P'[B0/$\mu_0 R_0^2$]

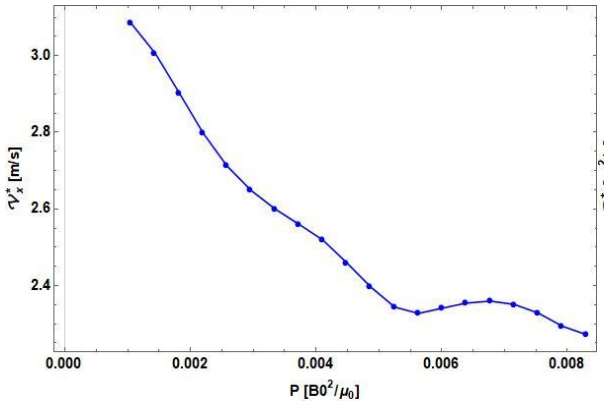
$\mathcal{V}_x^*$ [m/s]
P [$B0^2/\mu_0$]

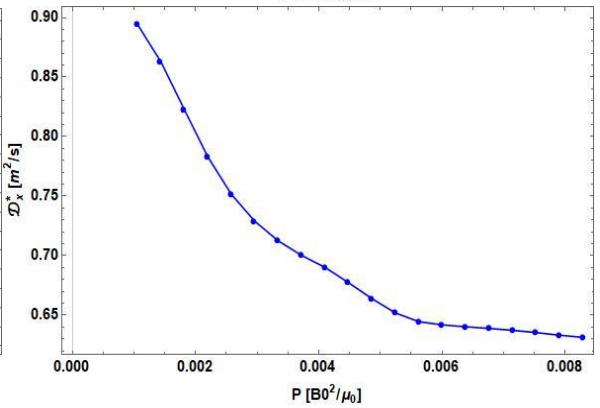
$\mathcal{D}_x^*$ [m^2/s]
P [$B0^2/\mu_0$]

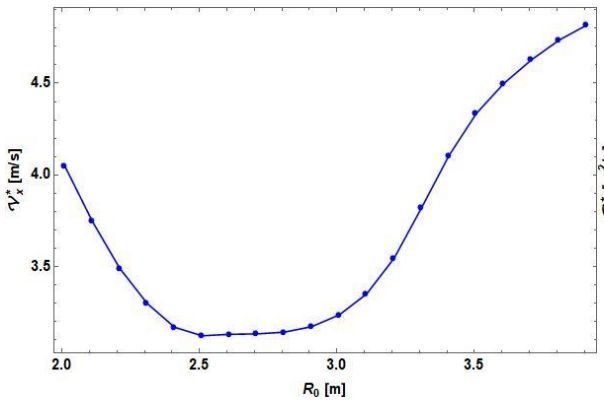
$\mathcal{V}_x^*$ [m/s]
R_0 [m]

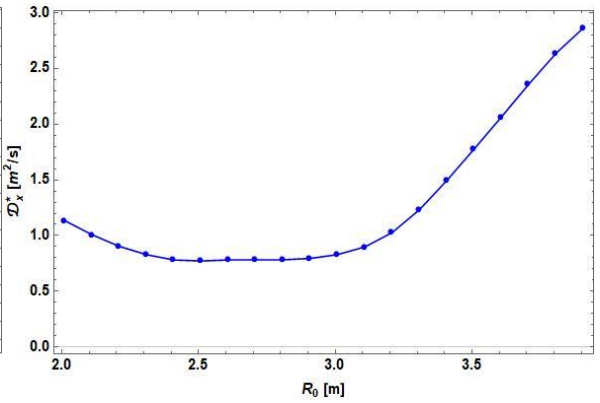
$\mathcal{D}_x^*$ [m^2/s]
R_0 [m]

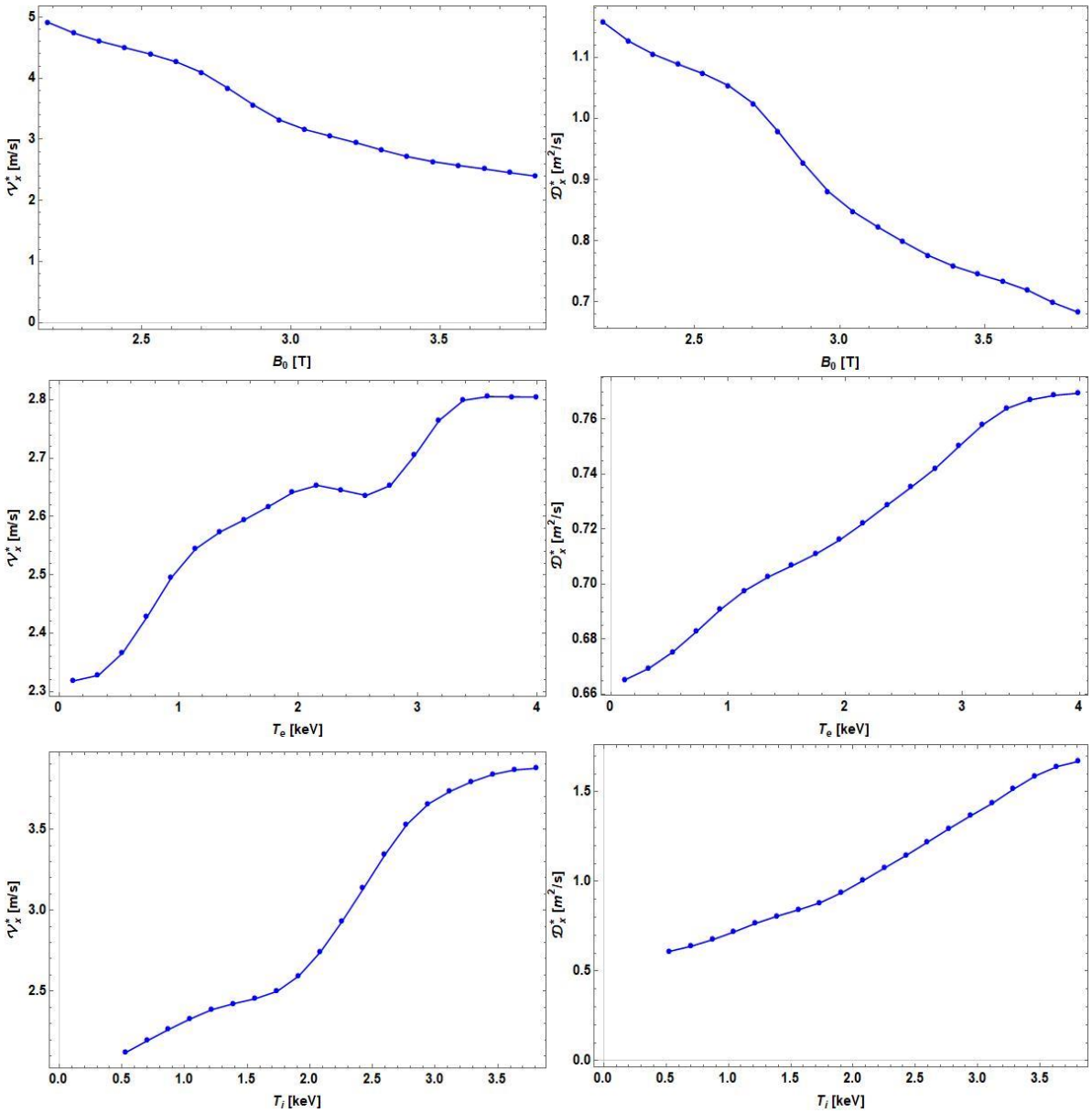

Fig. 8. Transport coefficients $V_x[m/s]$, $D_x[m^2/s]$ vs each free parameter of the database varied around the baseline configuration (see Table 1).

Similar results were obtained in an earlier stage of the project. However, the current results are qualitatively more accurate due to enhancements in the numerical T3ST code, many of which are minor and not detailed here. Additionally, the size of the database has been expanded. Regarding the validity of our results, it is important to note that the transport coefficients exhibit qualitatively correct trends, consistent with known analytical and numerical results from previous studies and the literature.

Bibliography

[1] Vlad M. and Spineanu F. Hidden drifts in turbulence Europhysics Letters (EPL) 124, 60002 (2018).

[2] Vlad M. and Spineanu F. Combined effects of hidden and polarization drifts on impurity transport in tokamak plasmas Phys. Plasmas 25, 092304 (2018).

[3] Vlad M., Palade D. I. and Spineanu F. Effects of the parallel acceleration on heavy impurity transport in turbulent tokamak plasmas. Plasma Phys. Control. Fusion 63, 035007 (2021).

[4] Vlad, M., Spineanu, F., Misguich, J.H. and Balescu, R. Diffusion with intrinsic trapping in two-dimensional incompressible stochastic velocity fields. Phys.Rev.E 58, 7359 (1998).

[5] Vlad M., Spineanu F. Trajectory structures and transport. Phys. Rev. E 70, 056304 (2004).

[6] Palade D. I. and Vlad M. Fast generation of Gaussian random fields for direct numerical simulations of stochastic transport, Statistics and Computing 31, 60 (2021).

[7] Palade D. I. Predicting the turbulent transport of cosmic rays via neural networks, Journal of Cosmology and Astroparticle Physics 2024 (01), 002

[8] DI Palade, LM Pomârjanschi, M Ghiţă, Scaling laws of two-dimensional incompressible turbulent transport, Physica Scripta 99 (1), 015201

[9] Palade D. I., Vlad M. and Spineanu F. Turbulent transport of the W impurity ions in tokamak plasmas: properties derived from a test particle approach. Nuclear Fusion 61, 116031 (2021).

[10] DI Palade, Peaking and hollowness of low-Z impurity profiles: an interplay between ITG and TEM induced turbulent transport", Nuclear Fusion 63 (4), 046007 (2023)

[11] DI Palade, L Pomârjanschi, Effects of intermittency via non-Gaussianity on turbulent transport in magnetized plasmas", Journal of Plasma Physics 88 (2), 905880202, (2022)

[12] L. M. Pomârjanschi, Neural networks for turbulent transport prediction in a simplified model of tokamak plasmas", Plasma Physics and Controlled Fusion 66.6 (2024): 065007.

[13] DI Palade, L Pomârjanschi, Effects of intermittency via non-Gaussianity on turbulent transport in magnetized plasmas, Journal of Plasma Physics 88 (2), 905880202, (2022)

[14] Vlad, M. and Spineanu, F. Random and quasi-coherent aspects in particle motion and their effects on transport and turbulence evolution. New J. Phys. 19 025014 (2017).

Acknowledgement

This work has been carried out within the framework of the EUROfusion Consortium, funded by the European Union via the Euratom Research and Training Programme (Grant Agreement No 101052200 — EUROfusion). Views and opinions expressed are however those of the author(s) only and do not necessarily reflect those of the European Union or the European Commission. Neither the European Union nor the European Commission can be held responsible for them.

The research work presented here has been developed together people from Consortio RFX, Padua, Italy (A. Murari).

Conclusion

We present here the extensive work undertaken to enhance our numerical capabilities. The T3ST code has been upgraded through the correction of minor issues and the addition of a new routine capable of fully and accurately integrating the collisional operators and realistic magnetic equilibria—both of which are critical components of ion dynamics. A series of analytical, numerical, and qualitative tests have been conducted on the new version of the code to verify the correctness of the results at both individual and statistical levels. Applied to a range of parameter configurations, the code has been used to perform numerical simulations and generate a database of results related to turbulent transport. This database will serve as a foundation for future work, including the validation of the code and its integration with machine learning tools, such as neural networks.

A numerical code was developed for connecting the test mode and the test particle investigations of the turbulence and transport. Both these analyses have the characteristics of the turbulence as input information. They determine the statistics of ion trajectories, the growth rates and the frequencies of the test modes as function of the input description of the turbulence. These studies were combined in an iterated approach, which is able to provide self-consistent results. It can be applied only for simple confining geometries, but complex nonlinear effects can be analyzed. We conclude that the code is a very useful tool for understanding the complex effects of trajectory coherence.